The Gamma-ray Transients Monitor (GTM) on board Formosat-8B and its GRB detection efficiency

Hsiang-Kuang Chang [a,b,c,*], Chi-Hsun Lin [d], Che-Chih Tsao [e], Che-Yen Chu [a],
Shun-Chia Yang [f], Chien-You Huang [b], Chao-Hsi Wang [a], Tze-Hsiang Su [b],
Yun-Hsin Chung [a], Yung-Wei Chang [g], Zi-Jun Gong [e], Jr-Yue Hsiang [a], Keng-Li Lai [e],
Tsu-Hsuan Lin [b], Chia-Yu Lu [e], Chien-Ying Yang [a]

[a] *Institute of Astronomy, National Tsing Hua University, Hsinchu, Taiwan*
[b] *Department of Physics, National Tsing Hua University, Hsinchu, Taiwan*
[c] *Center for Informatics and Computation in Astronomy (CICA), National Tsing Hua University, Hsinchu, Taiwan*
[d] *Institute of Physics, Academia Sinica, Taipei, Taiwan*
[e] *Department of Power Mechanical Engineering, National Tsing Hua University, Hsinchu, Taiwan*
[f] *Department of Electrical and Computer Engineering, National Yang Ming Chiao Tung University, Hsinchu, Taiwan*
[g] *Department of Physics, National Central University, Taoyuan, Taiwan*

Abstract

The Gamma-ray Transients Monitor (GTM) is a secondary payload on board Formosat-8B (FS-8B), a Taiwanese remote-sensing satellite scheduled to launch in 2024. The goal of GTM is to monitor Gamma Ray Bursts (GRBs) and other bright gamma-ray transients in the energy range from 50 keV to 2 MeV. GTM consists of two identical modules located on two opposite sides of FS-8B. Each module has four sensor units facing different directions to cover half of the sky. The two modules will then cover the whole sky, including the direction occulted by the Earth. Each sensor unit is composed of a GAGG scintillator array (50 mm × 50 mm × 8 mm) to be readout by SiPM with 16 pixel-channels. We describe the instrument design and its GRB detection efficiency in this paper. GTM is expected to detect about 40 GRBs per year.

1. Introduction

Gamma Ray Bursts (GRBs) were discovered more than half a century ago (Klebesadel et al., 1973). The nature of GRBs remained highly mysterious since then until the detection of their multi-wavelength afterglows and host galaxies in late 90's (Costa et al., 1997; van Paradijs et al., 1997; Frail et al., 1997), which eventually allowed to measure the redshift of GRBs and to establish their cosmological distance scale. Thereafter, thanks to the enormous observational progress and great theoretical efforts, ultra-relativistic jets from collapsars or NS-NS (NS-BH) mergers quickly developed and became the 'standard' model for long and short GRBs (see, e.g., Meszaros (2002, 2019) for GRB theory reviews). For GRBs with measured redshifts, strong correlations between the peak energy and other quantities, such as the isotropic energy release (Amati et al., 2002), the beaming-corrected energy

---

* Corresponding author at: Institute of Astronomy, National Tsing Hua University, Hsinchu, Taiwan.

E-mail address: hkchang@mx.nthu.edu.tw (H.-K. Chang).

release (Ghirlanda et al., 2004), and the peak luminosity (Yonetoku et al., 2004), were discovered. The large red-shifts make it possible to exploit these correlations for constraining cosmological parameters (Ghirlanda et al., 2004; Dai et al., 2004; Amati et al., 2008; Amati and Della Valle, 2013; Izzo et al., 2015; Demianski et al., 2017a; Demianski et al., 2017b). There are also efforts to develop refined schemes for the GRB long/short dichotomy based on these energy relations (e.g., Zhang et al. (2018)). Besides, the identification of GRB 170817A, a short GRB, with GW 170817, a gravitational wave event caused by merger of two neutron stars (Abbott et al., 2017a; Abbott et al., 2017b), provided strong supporting evidence to the merger models of short GRBs and opened the era of multi-messenger astronomy. Other similar GW events, e.g. GW 190425 (Abbott et al., 2020a) and GW 190814 (Abbott et al., 2020b), however, are not associated with any GRB, and the event in 2017 remains unique.

To further advance our understanding of all the above issues, more GRB monitors to provide larger sky coverage and better location capability, so that more GRBs, their afterglows and host galaxies, and their redshifts can be found, are very much desired.

The Gamma-ray Transients Monitor (GTM) on board Formosat-8B (FS-8B) is designed to monitor cosmic gamma-ray transients, most of which are GRBs, solar flares and magnetar bursts. FS-8B is the second of six Formosat-8 remote sensing satellites, which are built by the National Space Organization (NSPO) of Taiwan. FS-8B is scheduled to launch into a low-altitude (561 km), high-inclination (97.64°), sun-synchronous Earth orbit in 2024. GTM is the secondary payload of FS-8B. Its power and mass budget is 2 W (orbital average) and 2 kg, respectively. GTM will operate only when the remote sensing payload is off. The expected GTM operation duty cycle is about one third. Although GTM is a small instrument, it helps to enhance sky coverage for GRB monitoring and can also provide independent GRB location measurement, which may be exploited in synergy with other missions. In the following we describe GTM instrument design and its GRB detection efficiency. More details on GTM instrument testing measurements and GTM's GRB location capability will be reported in a future paper.

2. The GTM instrument

GTM consists of two almost identical modules on two opposite sides of the spacecraft bus, as shown with two red boxes in Fig. 1. Each module is about 10 cm × 10 cm × 8 cm in size. There are four sensor units facing different directions in each module, as shown in the upper left panel in Fig. 2. The eight sensor units altogether provide a 4π FoV, including the directions occulted by the Earth. The determination of the transient direction will be done in a way similar to that adopted by CGRO/BATSE (Pendleton et al., 1999) and Fermi/GBM (Connaughton et al., 2015; Goldstein et al., 2020), based on different fluxes
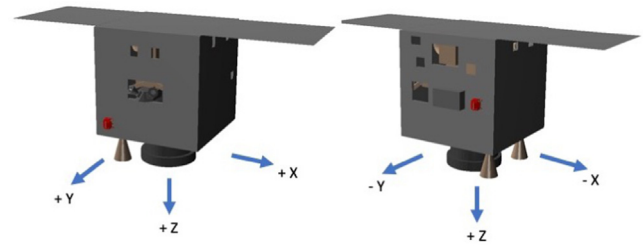

Fig. 1. GTM module locations on the FS-8B spacecraft bus. The two modules are shown with two red boxes on the $+Y$ and $-Y$ sides, each about 10 cm × 10 cm × 8 cm in size. The $+Z$ direction is defined to be the pointing direction of the remote sensing payload of FS-8B.
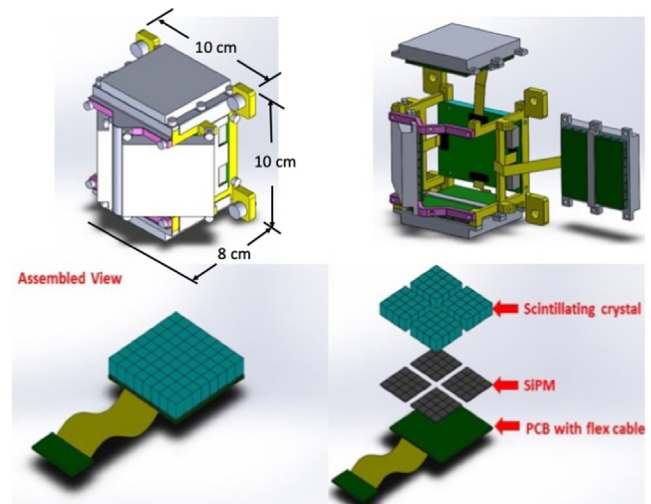

Fig. 2. The GTM module and sensor unit. The upper left panel shows a module with four sensor units facing four different directions (top, bottom, left (45° tilted) and right) to cover a hemisphere. The side without a sensor is the side to attach to the bus. The upper right panel shows the interior of the module. The four sensor units are connected to the mother readout board, which is on the side towards the bus and is shown here in green at the center. The two lower panels show the sensor unit. The whole scintillator array is about 50 mm × 50 mm × 8 mm. Some more details are in the main text.

measured by different sensor units. Efforts to assess GTM performance in this regard are on-going and the results will be reported at a later time.

The major part of each sensor unit is a scintillator array, of which the material we employ for GTM is Gadolinium Aluminum Gallium Garnet (GAGG). GAGG is non-hydroscopic. Its density is 6.63 g/cm^3, light yield about 56,000 photons/MeV, decay time about 100 ns, and energy resolution about 6% at 662 keV. Compared to that, among other scintillators, NaI and CsI have smaller densities and longer decay time. NaI has a much smaller light yield and is hydroscopic. LYSO has a larger density but much smaller light yield and a poorer energy resolution. CeBr$_3$ or LaBr$_3$ may be a good choice, but they are more expensive and both hydroscopic (see, e.g., Gostojić et al. (2016), Yoneyama et al. (2018)). With all these considerations and budget limitation, we decided to use GAGG as the scintillator material for GTM.

The scintillator array is composed of four sub-arrays, as shown in the lower right panel in Fig. 2. One sub-array consists of 16 GAGG bars, 6 mm × 6 mm × 8 mm each, in a 4 × 4 configuration to form 16 pixels with 6 mm × 6 mm in size for a pixel. Each GAGG bar is surrounded with 0.2-mm-thick $BaSO_4$ on the top and the four long sides as the scintillation-light reflection layers. Each sub-array is wrapped with a 0.05-mm aluminum film on the top and four sides. At the bottom of the sub-array, an SiPM of the same pixel size (Hamamatsu S13361-6050NE-04) is attached to convert scintillation light to electrical signals. Four sets of GAGG sub-arrays with SiPM are put together on a PCB for electrical signal output. The sensor unit is enclosed in an aluminum cover of 1-mm thickness on the top and 2-mm on the four sides. A thermal pad of thickness about 0.38 mm (Parker Chomerics 1671) is inserted between the GAGG array and the aluminum cover. The aluminum cover is part of the whole mechanical structure of the module.

The face-on effective area (photons coming from the top) of one GAGG sensor unit with its aluminum cover is shown in Fig. 3. It was obtained with Monte Carlo simulations. All the simulations in this work were conducted with a Geant4-based simulation toolkit, the Medium Energy Gamma-ray Astronomy Library (MEGAlib; Zoglauer et al. (2008)). Although the effective area in the energy range right below 50 keV is still significant, the $BaSO_4$ X-ray peak appearing around 35 keV (see Fig. 4) will make the data noisier around that energy. We therefore consider GTM to be sensitive in the energy range from 50 keV to 2 MeV. One may, however, use that 35-keV peak for the purpose of on-board calibration if the readout energy threshold can be set at below 20 keV or so. The currently expected readout threshold is 15 keV.
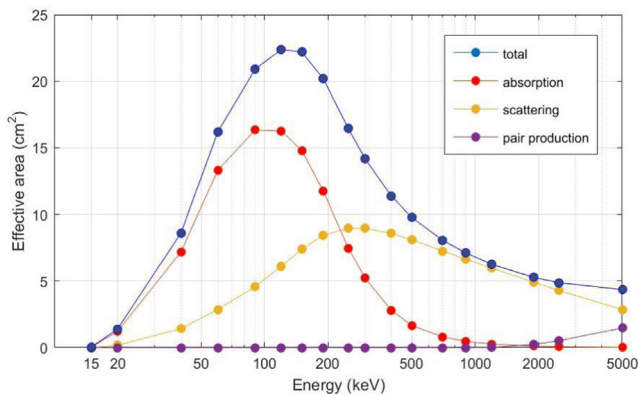

Fig. 3. The simulated face-on effective area (photons coming from the top) of one GTM sensor unit, which includes the aluminum cover, thermal pad, GAGG scintillator, SiPM and PCB as described in the main text. Contribution to the effective area includes photon-absorption, Compton scattering and pair production events, which are plotted in different colors. The effective area is suppressed at the low-energy end, essentially down to zero below 15 keV, because the aluminum cover, thermal pad, and $BaSO_4$ wrapping, which are all passive materials in the sensor unit, block out those low energy photons. The 1-σ statistical uncertainty in this simulation is 0.1%, which is smaller than the symbol size in this plot.
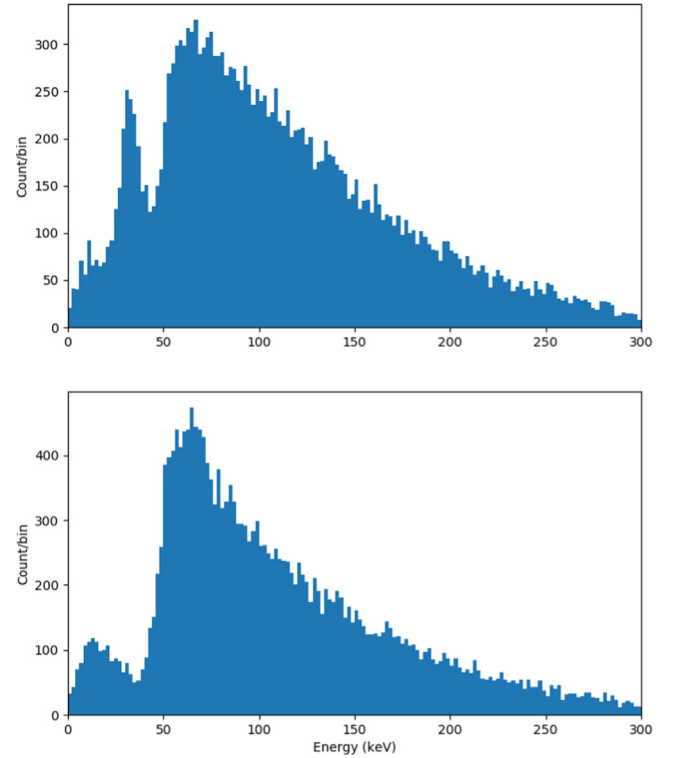

Fig. 4. Simulated response of one GTM sensor unit (upper panel) and that with all $BaSO_4$ removed (lower panel). The ordinate is in counts per 2-keV energy bin. The input photons are from the top of the detector with a cut-off power-law spectrum of parameters $\alpha = -1, E_p = 300$ keV (the photon number flux density $N_E \propto E^\alpha \exp(-E(2+\alpha)/E_p)$), typical for a long GRB. The input model is a constant source of 10-s duration and has a fluence of 4×10^{-4} erg/cm² in the range from 10 keV to 1 MeV. For this simulation we use input photons only in the energy range from 50 keV to 300 keV. The upper panel shows the response of a GTM sensor unit under such an exposure. To confirm the origin of the peak around 35 keV, we remove all the $BaSO_4$ in the detector mass model and show the detector response under the same exposure. It is clear that the peak around 35 keV is due to the presence of Ba in $BaSO_4$. In fact that is a combination of two Ba X-ray peaks at 32 and 36 keV. Because of the coarse spectral resolution of GAGG, which we set as 7.5% FWHM at 662 keV and scaling with $1/\sqrt{E}$, resulting in a 11.4-keV FWHM at 35 keV, those two peaks cannot be distinguished and appear as a single peak around 35 keV.

The whole GAGG array has 8 × 8 pixels. Limited by the power budget, however, four (2 × 2) pixels are bundled into one channel so that there are in total 16 readout channels for one sensor unit. A mother readout board in each module processes the signals coming from the four sensor units and communicates with the spacecraft bus. More details of the hardware and their testing measurement will be reported in another paper. Solely for the detection and location of GRBs one readout channel per sensor units will be enough. In the GTM design, within the power budget limit, we would like to retain 16 readout channels to better record spatial information of each interaction in the detector volume so that polarization measurement could be possible for very bright events. The polarization measurement will be conducted with the method similar to that described in Lowell et al. (2017) and Yang et al. (2018, 2020).

Together with GTM's testing measurement and location capability, the performance of GTM's polarization determination will be reported in a future paper.

3. GTM's GRB detection efficiency

To evaluate GTM's sensitivity, that is, how many GRBs it can detect within, say, one year, a detection efficiency study was conducted. Besides in-orbit background, this efficiency depends on many factors, such as source direction, satellite attitude, and source count rates. The latter depends on GRB fluence, duration, spectrum and burst light curves. To simplify the study so that a rough picture of GTM's GRB detection efficiency can be obtained, we use a square function to represent the light curve. The duration, i.e., the width of the square function, is chosen to be 10 s and 0.5 s for long and short GRBs, respectively. A cut-off power-law spectrum for the photon number flux density ($N_E \propto E^\alpha \exp(-E(2+\alpha)/E_p)$) is assumed, with the photon index α and the peak energy E_p chosen to be $\alpha = -1, E_p = 300$ keV and $\alpha = -0.5, E_p = 500$ keV for long and short GRBs, respectively. These numbers are the median of t_{50} and corresponding spectral parameters of Konus-WIND-detected GRBs (Svinkin et al., 2016; Tsvetkova et al., 2017).

3.1. Source and background count rates

With the aforementioned assumptions for GRB sources, we choose four source directions to study, all with a polar angle $\theta = 45°$. The azimuthal angles are $\phi = \pm 60°$ and $\phi = \pm 120°$ in the spacecraft coordinates. The zero polar angle $\theta = 0°$ is in the $-Z$ direction (see Fig. 1) and and the azimuthal angle starts from the $-X$ direction ($\phi = 0°$), increasing towards the $+Y$ direction. These four source directions are so chosen that they are arbitrary

and usual in the sense that they do not correspond to any symmetric axis of any of the eight sensors.

We estimate the source count rates in the time interval when the GRB is on with simulations using a large fluence, whose results can be scaled down to obtain the count rates for smaller fluences. In such a case, simulation uncertainties are reduced for cases of small fluences. Equivalently, one may also use a longer simulation exposure time (longer than the duration) to achieve smaller statistical uncertainties in estimating the count rates. The simulation input photons are from 10 keV to 10 MeV. For all the count rates, we consider only those photons whose deposit energy in the detectors is between 50 keV and 300 keV, in which the detectors have better response.

The count rates of each individual detectors are listed in Table 1, for which the fluences are set at 4×10^{-4} erg/cm^2 and 1×10^{-5} erg/cm^2, both in the energy range from 10 keV to 1 MeV, for long and short GRBs, respectively. One should note that these count rates are for GRBs with a very large fluence. The one for long GRBs is at the high end of the fluence distribution of Fermi/GBM-detected GRBs. Only four GRBs with a fluence larger than that were detected during year 2008–2018. The one used for short GRBs is right beyond all the detected short GRBs up to date (von Kienlin et al., 2020). One can easily scale down the count rates for smaller fluences.

To estimate the in-orbit background, we employed a low-altitude (561 km), high-inclination (97°) polar Earth-orbit radiation background model incorporated in MEGA-lib for our simulation. It includes cosmic photons, protons, α particles, electrons and positrons, and albedo photons, protons, neutrons, electrons, and positrons. The dependence on incident directions (zenith angles) of each component is taken into account. The energy range of the input background model is from 10 keV to 1 TeV. Trapped components are not included. The estimate is therefore only good for orbits away from SAA and polar regions. Since

Table 1

Simulated GRB count rates for each GTM sensor. All the count rates are in units of counts per second and are in the energy range from 50 keV to 300 keV. Each sensor is denoted with two capital letters. The first letter with 'N' refers to the GTM module on the negative Y side of the spacecraft and 'P' to the positive one. The second letter with 'N' refers to the sensor facing more to the negative X direction, 'P' to the positive X direction, 'T' ('top') to the negative Z direction, and 'B' ('bottom') to the positive Z direction. The statistical uncertainty of this simulation is that the count rates in this table with a two-digit number have two significant digits and all the others have three significant digits. The background count rate per sensor in the same energy range is 42.6 cps. See Section 3 for more details.

Angle ϕ	NN	NP	NT	NB	PN	PP	PT	PB
Long GRBs (with fluence equal to 4×10^{-4} erg/cm^2, duration 10 s)								
$+60°$	55	63	91	73	1520	745	1690	539
$-60°$	1540	789	1730	595	55	63	71	72
$+120°$	44	41	72	46	723	1530	1710	534
$-120°$	737	1530	1730	595	23	19	25	24
Short GRBs (with fluence equal to 1×10^{-5} erg/cm^2, duration 0.5 s)								
$+60°$	33	34	50	42	576	319	651	241
$-60°$	612	342	680	272	33	32	41	46
$+120°$	24	27	45	25	299	591	675	242
$-120°$	217	621	666	250	12	11	14	12

the spacecraft can have different attitude when GRBs occur, we adopt the configuration that the zenith is in the $-Z$ direction of the spacecraft and take the background count rates averaged over the eight detectors as the background count rate for each detector, which we found to be 42.6 cps in the energy range from 50 keV to 300 keV. In the next subsection we use this background count rate and the source count rates in Table 1 scaled down to different fluences to study GTM's GRB detection efficiency as a function of fluences.

3.2. The search algorithm and detection efficiency

GTM will be in operation only when the remote sensing payload of FS-8B is off and the spacecraft is away from SAA and polar regions. Data transmission from the spacecraft to the ground is expected to be about four times per day. GTM science data will therefore be composed of segments of time intervals of different lengths. The search algorithm described in the following will be applied on ground to the data right after data is down linked. For the current study, we create artificial data of 1 ksec, which contain a GRB event of a certain fluence at a random epoch. This artificial data is represented by eight light curves, one for each detector, created with given background and source count rates and Poisson random fluctuations. We then apply a search algorithm to see whether the event is detected. The whole procedure is repeated for 10,000 times. The detection efficiency can therefore be obtained.

To search for burst events, we first bin the 1-ksec artificial data set for a certain sensor into a light curve with 1-ms time bins. The average count number per time bin is computed to be the background level, that is, we assume a constant background, which is true for the current artificial data. For real data in the future, a low-order polynomial will be employed to account for possible background variation in the orbit. We then examine each time bin to check whether the count number in that time bin is higher than the number deviating from the background level at a Poisson random probability lower than 10^{-3}. If it is higher, the detection of a burst is reported. If there is no detection, we adopt a half-bin shift, that is, a 0.5-ms shift for the current case, to produce a new light curve, still with 1-ms time bins, to repeat the search. If the is still no detection, the above procedure is repeated with a larger time bin. Currently we use 2 ms, 5 ms, 10 ms, 20 ms, 50 ms, 100 ms, 200 ms, 500 ms, 1 s, 2 s, 5 s and 10 s as the bin size for the search. The whole procedure is applied to the data set of each sensor unit separately. If there is no detection after all these searches, the data sets of the four sensor units in one GTM module are combined and the search algorithm is applied again. For real data in the future, burst search will be conducted with all the different time-bin sizes on the whole data set, even when there is a burst detection reported at a certain epoch with a certain bin size, so that

bursts separated in time in the same data set won't be missed. All the bins satisfying the burst detection criterion will be flagged and further processing will be initiated to produce burst timing characteristics and burst location.

For the current detection efficiency study, the aforementioned procedure is repeated for 10,000 times for a GRB of a certain fluence from a certain direction. Their expected count rates for each GTM detectors can be derived from Table 1. The detection efficiency is defined to be the fraction of successful detection in the 10,000 simulations, which is shown in Fig. 5 as a function of fluences. We can see that the 50% detection efficiency happens at a fluence of 3.4×10^{-6} erg/cm^2 and 2.5×10^{-6} erg/cm^2 for long and short GRBs, respectively. A more stringent threshold
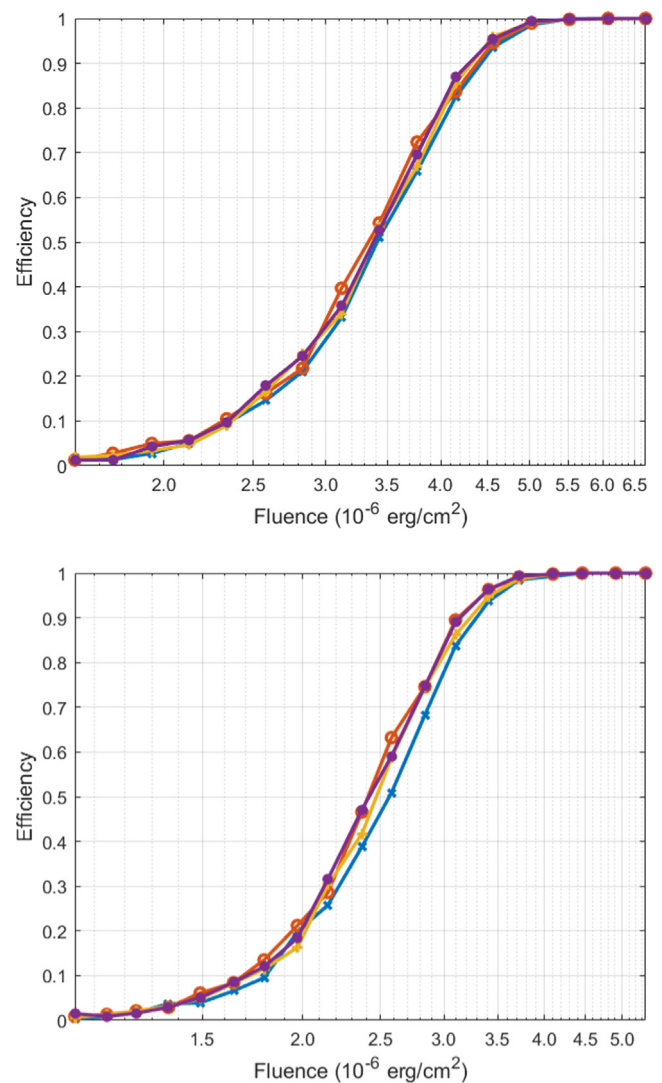

Fig. 5. GTM's GRB detection efficiency as a function of fluences. The upper panel is for long GRBs and the lower for short ones. The four almost identical curves in both panels are for GRBs from four directions described in the main text. The 50% detection efficiency is at a fluence of about 3.4×10^{-6} erg/cm^2 for long GRBs and 2.5×10^{-6} erg/cm^2 for short ones. The random probability threshold is set at 10^{-3} for the burst search in the algorithm.

at 10^{-4} only leads to a slightly lower efficiency, with the 50% detection efficiency happening at 3.9×10^{-6} erg/cm^2 and 2.8×10^{-6} erg/cm^2 for long and short GRBs, respectively. Fermi/GBM detected about 1200 long and 30 short GRBs of fluences larger than that in 10 years (von Kienlin et al., 2020). The probability thresholds at 10^{-3} and at 10^{-4} do not really make a difference. Since GTM has only a 36% duty cycle, we expect GTM to detect about 43 long and 1 short GRBs in one year.

Since we treat the fluence of an event, in the current study, as contained in a square-function light curve with a t_{50} width, the count rate we obtain from simulation is larger than the average count rate of that event. It is reasonable to do so for triggering search, although real peak count rate may still be much larger and we are in fact somewhat underestimating the chance of success for triggering.

4. Summary

The Gamma-ray Transients Monitor (GTM) is an all-sky monitor, sensitive in the energy range from 50 keV to 2 MeV. It is a secondary payload on board Formosat-8B, which is scheduled to launch in 2024. GTM is expected to detect about 40 GRBs per year and some brighter solar flares and magnetar bursts. It will contribute to enhance the sky coverage for GRB monitoring. GTM's capability of GRB location determination and polarization measurement is being studied and will be reported in a future paper.

Declaration of Competing Interest

The authors declare that they have no known competing financial interests or personal relationships that could have appeared to influence the work reported in this paper.

References

Abbott, B.P., Abbott, R., Abbott, T.D., et al., 2017a. Multi-messenger Observations of a Binary Neutron Star Merger. ApJL 848, L12.

Abbott, B.P., Abbott, R., Abbott, T.D., et al., 2017b. Gravitational Waves and Gamma-Rays from a Binary Neutron Star Merger: GW170817 and GRB 170817A. ApJL 848, L13.

Abbott, B.P., Abbott, R., Abbott, T.D., et al., 2020a. GW190425: Observation of a Compact Binary Coalescence with Total Mass $\sim 3.4 M_\odot$. ApJL 892, L3.

Abbott, R., Abbott, T.D., Abraham, S., et al., 2020b. GW190814: Gravitational Waves from the Coalescence of a 23 Solar Mass Black Hole with a 2.6 Solar Mass Compact Object. ApJL 896, L44.

Amati, L., Frontera, F., Tavani, M., et al., 2002. Intrinsic spectra and energetics of BeppoSAX Gamma-Ray Bursts with known redshifts. A&A 390, 81–89.

Amati, L., Guidorzi, C., Frontera, F., Della Valle, M.D., Finelli, F., Landi, R., Montanari, E., 2008. Measuring the cosmological parameters with the $E_{p,i}$-E_{iso} correlation of gamma-ray bursts. MNRAS 391, 577–584.

Amati, L., Della Valle, M., 2013. Measuring Cosmological Parameters with Gamma Ray Bursts. Int. J. Mod. Phys. D 22, 1330028.

Connaughton, V.C., Briggs, M.S., Goldstein, A., et al., 2015. Localization of Gamma-Ray Bursts Using the Fermi Gamma-Ray Burst Monitor. ApJS 216, 32.

Costa, E., Frontera, F., Heise, J., et al., 1997. Discovery of an X-ray afterglow associated with the γ-ray burst of 28 February 1997. Nature 387, 783–785.

Dai, Z.G., Liang, E.W., Xu, D., 2004. Constraining Ω_M and Dark Energy with Gamma-Ray Bursts. ApJ 612, L101–L104.

Demianski, M., Piedipalumbo, E., Sawant, D., Amati, L., 2017a. Cosmology with gamma-ray bursts I. The Hubble diagram through the calibrated $E_{p,i}$?E_{iso} correlation. A&A 598, A112.

Demianski, M., Piedipalumbo, E., Sawant, D., Amati, L., 2017b. Cosmology with gamma-ray bursts Astronomy II. Cosmography challenges and cosmological scenarios for the accelerated Universe. A&A 598, A113.

Frail, D., Kulkarni, S.R., Nicastro, L., Feroci, M., Taylor, G.B., 1997. The radio afterglow from the γ-ray burst of 8 May 1997. Nature 389, 261–263.

Ghirlanda, G., Ghisellini, G., Lazzati, D., 2004. The Collimation-corrected Gamma-Ray Burst Energies Correlate with the Peak Energy of Their νF_ν Spectrum. ApJ 616, 331–338.

Ghirlanda, G., Ghisellini, G., Lazzati, D., Firmani, C., 2004. Gamma-Ray Bursts: New Rulers to Measure the Universe. ApJ 613, L13–L16.

Goldstein, A., Fletcher, C., Veres, P., et al., 2020. Evaluation of Automated Fermi GBM Localizations of Gamma-Ray Bursts. ApJ 895, 40.

Gostojić, A., Tatischeff, V., Kiener, J., et al., 2016. Characterization of LaBr$_3$: Ce and CeBr$_3$ calorimeter modules for 3D imaging in gamma-ray astronomy. Nucl. Instrum. Methods Phys. Res. A 832, 24–42.

Izzo, L., Muccino, M., Zaninoni, E., Amati, L., Della Valle, M., 2015. New measurements of Ω_m from gamma-ray bursts. A&A 582, A115.

Klebesadel, R.W., Strong, I.B., Olson, R.A., 1973. Observations of Gamma-Ray Bursts of Cosmic Origin. ApJ 182, L85–L88.

Lowell, A.W., Boggs, S.E., Chiu, C.-L., et al., 2017. Maximum Likelihood Compton Polarimetry with the Compton Spectrometer and Imager. ApJ 848, 120.

Meszaros, P., 2002. Theories of Gamma-Ray Bursts. ARAA 40, 137–169.

Meszaros, P., 2019. Gamma-Ray Bursts: theoretical issues and developments. Mem. S.A. It. 90, 57–66.

Pendleton, G.N., Briggs, M.S., Kippen, R.M., Paciesas, W.S., Stollberg, M., Woods, P., Meegan, C.A., Fishman, G.J., McCollough, M.L., Connaughton, V., 1999. The Structure and Evolution of LOCBURST: The BATSE Burst Location Algorithm. ApJ 512, 362–376.

Svinkin, D.S., Frederiks, D.D., Aptekar, R.L., Golenetskii, S.V., Pal'shin, V.D., Oleynik, Ph.P., Tsvetkova, A.E., Ulanov, M.V., Cline, T.L., Hurley, K., 2016. The Second Konus-Wind Catalog of Short Gamma-Ray Bursts. ApJS 224, 10.

Tsvetkova, A., Frederiks, D., Golenetskii, S., Lysenko, A., Oleynik, P., Pal'shin, V., Svinkin, D., Ulanov, M., Cline, T., Hurley, K., Aptekar, R., 2017. The Konus-Wind Catalog of Gamma-Ray Bursts with Known Redshifts. I. Bursts Detected in the Triggered Mode. ApJ 850, 161.

van Paradijs, J., Groot, P., Galama, T., et al., 1997. Transient optical emission from the error box of the γ-ray burst of 28 February 1997. Nature 386, 686–689.

von Kienlin, A., Meegan, C.A., Paciesas, W.S., et al., 2020. The Fourth Fermi-GBM Gamma-Ray Burst Catalog: A Decade of Data. ApJ 893, 46.

Yang, C.-Y., Lowell, A., Zoglauer, A., et al., 2018. The polarimetric performance of the Compton Spectrometer and Imager (COSI). Proc. SPIE 10699, 106992K.

Yang, C.-Y., Chang, Y.-C., Liang, H.-H., Chu, C.-Y., Hsiang, J.-Y., Chiu, J.-L., Lin, C.-H., Laurent, P., Rodriguez, J., Chang, H.-K., 2020. Feasibility of Observing Gamma-Ray Polarization from Cygnus X-1 Using a CubeSat. AJ 160, 54.

Yonetoku, D., Murakami, T., Nakamura, T., Yamazaki, R., Inoue, A.K., Ioka, K., et al., 2004. Gamma-Ray Burst Formation Rate Inferred from the Spectral Peak Energy-Peak Luminosity Relation. ApJ 609, 935–951.

Yoneyama, M., Kataoka, J., Arimoto, M., Masuda, T., Yoshino, M., Kamada, K., Yoshikawa, A., Satod, H., Usukid, Y., 2018. Evaluation of GAGG: Ce scintillators for future space applications. J. Instrum. 13, P02023.

Zhang, Z.B., Zhang, C.T., Zhao, Y.X., Luo, J.J., Jiang, L.Y., Wang, X.L., Han, X.L., Terheide, R.K., 2018. Spectrum-energy Correlations in GRBs: Update, Reliability, and the Long/Short Dichotomy. PASP 130, 054202.

Zoglauer, A., Andritschke, R., Boggs, S.E., Schopper, F., Weidenspointner, G., Wunderer, C.B., 2008. MEGAlib: simulation and data analysis for low-to-medium-energy gamma-ray telescopes. Proc. SPIE 7011, 70113F.